**Revisiting the Extended X-ray Absorption Fine Structure Fitting Procedure through a Machine Learning-Based Approach**

(Article begins on next page)

10 September 2024

Revisiting the Extended X-ray Absorption Fine Structure Fitting Procedure through a Machine Learning-Based Approach. J. Phys. Chem. A, 125, 2021, 7080–7091

DOI: 10.1021/acs.jpca.1c03746

# Revisiting the EXAFS Fitting Procedure through a Machine Learning-Based Approach

A. Martini[1,2(*)], A. L. Bugaev[1,3(*)], S. A. Guda[1,4], A. A. Guda[1], E. Priola[2,5], E. Borfecchia[2], S. Smolders[6], K. Janssens[6], D. De Vos[6] and A. V. Soldatov[1]

[1]The Smart Materials Research Institute, Southern Federal University, Sladkova 178/24, 344090 Rostov-on-Don, Russia

[2]Department of Chemistry, University of Torino, Via P. Giuria 7, 10125 Torino, Italy

[3]Southern Scientific Centre, Russian Academy of Sciences, Chekhova 41, 344006 Rostov-on-Don, Russia

[4]Institute of mathematics, mechanics and computer science, Southern Federal University, Milchakova 8a, 344090 Rostov-on-Don, Russia

[5]CrisDi, InterDepartemental Center for Crystallography, University of Turin, Italy

[6]Centre for Membrane separations, Adsorption, Catalysis and Spectroscopy for Sustainable Solutions (cMACS), Department of Microbial and Molecular Systems (M2S); KU Leuven, Celestijnenlaan 200F, post box 2454, 3001 Leuven (Belgium).

**Abstract**

A novel approach for the analysis of extended X-ray absorption fine structure (EXAFS) spectra is developed exploiting an inverse machine learning-based algorithm. Through this approach, it is possible to explore and account, in a precisely way, the non-linear geometry dependence of the photoelectron backscattering phases and amplitudes of single and multiple scattering paths. In addition, the determined parameters are directly related to the 3D atomic structure, without the need to use complex parametrization as in the classical fitting approach. The applicability of the approach, its potential and the advantages over the classical fit were demonstrated by fitting the EXAFS data of the two molecular systems, namely the $KAu(CN)_2$ and $[RuCl_2(CO)_3]_2$ complexes.

## 1. Introduction

Extended X-ray absorption fine structure (EXAFS) spectroscopy is an efficient element selective technique employed for the extraction of local atomic structural parameters, such as interatomic distances, coordination numbers and Debye-Waller (DW) factors.[1,2] In the experimental procedure, X-ray photons are used to excite a core-level electron whose final state is modified due to its backscattering from neighboring atoms, resulting in the oscillatory behavior of the X-ray absorption coefficient, $\mu(E)$, as a function of photon energy. The oscillatory part $\chi(k)$, extracted from $\mu(E)$ signal, can be described as a sum of an infinite number of scattering events $\chi_i(k)$:[1,3]

$$\chi(k) = \sum_{i=1}^{\infty} \chi_i(k) \tag{1}$$

with $\chi_i(k)$ defined as:

$$\chi_i(k) = S_{0\,i}^2 \frac{N_i F_i(k)}{kR^2} \sin[2kR_i + \phi_i(k)] e^{-2\sigma_i^2 k^2} e^{-\frac{2R_i}{\lambda_i(k)}} \tag{2}$$

where $k$ denotes the excited photoelectron wavevector, $2R_i$ is the total scattering path length, $N_i$ is the number of scattering paths equivalent to the selected one (i.e. the path degeneracy), $\sigma_i^2$ is the DW factor associated with the $i^{th}$ scattering event. The terms $F_i$ and $\phi_i$ are the path backscattering amplitude factor and phase shift. $S_{0\,i}^2$ is a many body reduction factor accounting for the amplitude damping due to multi-electron effects (intrinsic losses), while $\lambda_i(k)$ is the mean free path of the $i^{th}$ photoelectron.

Eq. (1) involves different contributions stemming from single scattering (SS) paths, when the photoelectron is backscattered by one neighbouring atom, and multiple scattering (MS) paths, when several atoms are involved in the scattering process. The latter ones contain information not only about the bond distances but also about the bond angles. However, due to the typically large path length, their contribution becomes significant only at high $k$-values due to characteristic behaviour of $\lambda_i(k)$.[4] For practical implementation, the infinite series in eq. (1) is always limited by the half path length $R_i$ and by the significance of the $\chi_i(k)$ contribution on the resulting EXAFS signal.[5] In the typical implementation provided by the Artemis code (IFEFFIT),[6] an initial guess structure is used for the *ab initio* calculation of the scattering phases and amplitudes by the FEFF program,[7] which are subsequently used to fit the experimental oscillatory signal given by eq. (1) refining $S_0^2$ and $R_i$, $N_i$ and $\sigma_i$ for each selected path of eq. (2).

Although being well developed and successfully applied over decades, the standard approach in the EXAFS analysis exhibits some drawbacks. First, it is important to consider that the scattering amplitudes, phases and electron mean-free paths depend on the actual atomic structure and become unreliable for big variations of the bond distances with respect to the initial guess structure. In addition, it is worth mentioning that for the MS paths, which are in many cases neglected in the analysis, these functions show a strong non-linear angular dependence especially in the case of

linear atomic chains.[5,8] The first attempt to solve this problem was provided by Frenkel et al.[9-12] In these works, the authors were able to estimate, from the analysis of certain double and triple forward MS paths, the average buckling angles proper of some mixed ionic salts. In particular, they demonstrate that it is possible to describe the buckling dependence for angles $\lesssim 20°$ by the expansion of the effective backscattering amplitudes factors of these MS paths around the average buckling angles provided by diffraction techniques. Further improvements to this problem were also provided in the $N$-body expansion of the GNXAS code[13,14] and by alternative methodologies represented by the classical (force-field based) molecular dynamics[15-17] or by the Reverse Monte Carlo approach.[18,19]

The second problem is related to the choice of variables, appearing in eq. (2), which can be properly refined through the fitting procedure, since the maximum number of fitting parameters is limited according to the Nyquist criterion to $N_{idp} \approx 2\frac{\Delta k \Delta R}{\pi}$, where $\Delta R$ and $\Delta k$ are the fitting range in the direct ($R$) space and the $k$-interval used for the Fourier transform, respectively.[20,21] Furthermore, as the number of parameters involved in the fit increase, the correlation among all the couples of the fitting variables becomes higher. These two facts frequently lead to the necessity to express some fitting variables, especially those linked to MS paths in eq. (2), as a function of parameters already involved in the EXAFS fit within a simpler SS model.[22] Apart from technical complications and the absence of a common *modus operandi* in the field, the conversion of the fitting parameters into the exact 3D representation of the atomic structure is not straightforward.

In the pioneering works of Timoshenko *et al.*[23,24] the possibility to exploit a Machine Learning (ML) approach for the quantitative analysis of EXAFS spectra was demonstrated. In particular, the authors have constructed determined artificial neural-networks that allowed to predict, starting

from certain experimental spectra, the two-body radial distribution functions (also partial) related to different atoms composing metal bulk materials and mono/bi-metallic nanoparticles.

Herein, we propose an alternative EXAFS fitting procedure exploiting an *indirect* ML-based approach. Herein, the term *indirect* [25] is used to indicate that a certain ML algorithm is used to predict, from a certain set of user defined structural parameters, those path signals assumed to influence more the related experimental EXAFS spectrum. More specifically, our method extends the multidimensional interpolation approach, proposed originally by Smolentsev *et al* in FitIt code[26] and recently improved by our group in the new PyFitIt code,[27] from the XANES to the EXAFS case. A theoretical training set is employed to construct a series of implicit functions approximating each scattering path $\chi_i(k)$ under the continuous variation of some pre-defined parameters. Eq. (1) is then generalised to account for any kind of deformations: from the bonds stretching to the variation of multiple angles of the selected molecular structure, including significant deviations from the initial molecular geometry. Moreover, the effective path lengths associated to each scattering process are obtained directly as a function of the selected molecular deformations without recurring to any elaborated formula. The proposed approach is successfully applied to analyse the experimental EXAFS data of $KAu(CN)_2$, and $[RuCl_2(CO)_3]_2$ molecular complexes, in which the advantages over the classical fit are demonstrated.

## 2. Methods

The basic idea, behind our approach, stands in the construction, for each scattering process, of a signal path function $\chi_i$ that, under the variation of a user-defined set of $n$ structural parameters, $\boldsymbol{p} = (p_1, \ldots, p_n)$, is able to return an accurate approximation for the $i^{\text{th}}$ scattering signal. This contribution needs to be as close as possible to the one obtained through an *ab initio* calculation involving the molecular complex affected by $\boldsymbol{p}$. The choice of the structural parameters $\boldsymbol{p}$ to be refined depends exclusively on the user preference. Clearly, a certain knowledge on the system under study is required to avoid the variation of determined geometric parameters, which, rarely, can undergo towards certain kind of deformations. A good example is represented by the double or triple bond distances connecting two atoms, which generally should be maintained almost unperturbed, as showed in the example reported in **Section 3.1**.

The perturbation of each element of $\boldsymbol{p}$ is reflected automatically in the change of each vector distances $\{\boldsymbol{r}\}_i = (\boldsymbol{r}_1, \ldots, \boldsymbol{r}_m)$, where $\boldsymbol{r}_m$ is the coordinates vector of the $m^{\text{th}}$ atom involved in the scattering process depending on $\boldsymbol{p}$. It follows that, for a given $\chi_i$ path, the amplitude, the phase and the electron mean free path can be described as non-linear functions of $\{\boldsymbol{r}(\boldsymbol{p})\}_i$: $F_i(k, \{\boldsymbol{r}(\boldsymbol{p})\}_i)$, $\phi_i(k, \{\boldsymbol{r}(\boldsymbol{p})\}_i)$ and $\lambda_i(k, \{\boldsymbol{r}(\boldsymbol{p})\}_i)$. These terms contribute to the path signal $\chi_i$, whose dependence from $\boldsymbol{p}$ can be then expressed as $\chi_i(k, \boldsymbol{p})$. For the sake of clarity, the variations of the scattering amplitudes and the total phase shifts for a selected SS and MS path are showed, in correspondence of controlled modification of the bond distances and of the angle α proper of the KAu(CN)$_2$ structure, in **Figure 2** of **Section 3.1** (*vide infra*).

The fitting procedure exploiting an ML approach can be formally divided in two parts, described in **Sections 2.1** and **2.2**, respectively. First, it is necessary to identify the paths with the highest impact on the total EXAFS signal. Secondly, a set of non-linear functions, approximating the

dependence of each $\chi_i$ signal from $\boldsymbol{p}$, are generated. This part foresees the training procedure of a ML algorithm. Once that all the selected $\chi_i(k)$ are approximated in the whole range of variation of $\boldsymbol{p}$, the theoretical total EXAFS signal is generated summing all the single contributions. Afterwards the fitting of the experimental spectrum can be performed.

*2.1. Generation of a set of ML-based $\chi_i$ functions*

Supervised ML algorithms requires a dataset of theoretical spectra linked (i.e. labeled) to the corresponding molecule geometry.[25,28] Regarding the proposed approach, only those scattering paths that contribute significantly in the selected region of the experimental spectrum are chosen for the training set generation. In the *classical* (geometry independent) EXAFS fit, this requirement can be satisfied considering the SS and MS paths having a curve-wave importance ratio (rank)[6,7] higher than a certain user defined value. In case of a geometry-variable molecular complex, this step requires a well-defined methodology if the most relevant EXAFS paths are not known beforehand. Some MS paths depend strongly on the geometry and can become relevant for certain deformations of the molecule. For example, the gradual evolution of a collinear MS path to a triangular-one can cause the abatement of its intensity, expressed in terms of its rank.[29] It follows that there could be some molecular configurations, involving the same atoms, where a MS path is significant while in the others its signal contribution is completely negligible. To consider this behavior, the following procedure is proposed.

In the range of variation of structural parameters $\boldsymbol{p}$ a *coarse* multidimensional grid is generated (see **Figure S1** in the Supporting Information (S.I.)). Afterwards, for each point of the grid, a FEFF calculation is executed, and the rank terms associated to each path are extracted and analyzed for each deformation. Only those paths possessing a rank equal or higher than 15% and a maximum half path length ($R_i$) of 5 Å are selected. This approach allows to consider all possible paths having

a strong impact on the fitting routine independently from the starting geometry. If necessary, further user-defined filtering criteria can be introduced to limit the number of paths. For example, if a relevant path (rank>15%) shows for each point of the *coarse* grid a $R_i$-value higher than the fitting range, it can be properly excluded. The number of significant paths is further refined selecting only those not *equivalent* to each other. The term *equivalent* is used here to indicate two or more paths possessing the same kind of scattering atoms, showing the same $R_i$ and scattering angles if evaluated on the same reference molecule (i.e. the initial unperturbed). The time-reversal symmetry[30] is taken in consideration too. In fact, in case of disagreement among the scattering angles associated to two paths presenting the same $R_i$ and atoms type, the comparison can be repeated inverting the order of the atoms involved in one of the scattering processes. A pictorial representation of the *equivalence* criterion defined before is depicted in **Figure S2**.

All the significant, not *equivalent* paths obtained through this procedure, will be further approximated as a function of the variation of $\boldsymbol{p}$ employing a regression approach. The latter is realized by means of an ML algorithm, which foresees a training procedure.

Herein, the multidimensional space of the configurations **P**, generated by all combinations of the chosen geometric parameters within their range of variation (i.e. $p_1 \times ... \times p_n$ ) is sampled uniformly according to the Improved Latin Hypercube Sampling (IHS) method.[31] This technique ensures the narrowest distance among the projections of each multidimensional point along every dimension of **P**.[25,27] The result is a *finer* multidimensional grid (in contrast to the precedent one, showed in **Figure S1**). For sake of clarity, **Figure S3** of the S.I. text shows the distribution of points employed to sample properly the space of possible configurations **P** associated to the example discussed in **Section 3.1**.

For every point of **P**, a distorted molecular complex is generated and a FEFF calculation is executed. This process is relatively fast. For both examples discussed in **Section 3**, the execution of the FEFF software for 500 input files (i.e. 500 perturbed geometries for both of the cases) took just few minutes. Afterwards, each path, which was assumed to be relevant in the precedent step, is identified among all the FEFF scattering processes through the equivalence criterion. Herein, the path attributes: $F_i(k)$, $\phi_i(k)$ and $\lambda_i(k)$ are extracted and employed to reconstruct the corresponding $\chi_i(k)$ signal.

At the end of this process, every not *equivalent* significant path possesses a ML training dataset containing the corresponding paths functions $\chi_i(k)$ evaluated for all the sampling points of **P**. As an example, **Figure S4** reports all the ML-training datasets employed to generate the corresponding paths functions exploited to fit the EXAFS spectrum of the KAu(CN)$_2$ complex described in **Section 3.1.**

Starting from these data-arrays, an Extra Trees regressor algorithm[25,27,28] is trained and, for each selected path and a multidimensional interpolating path function is generated: $\chi_i(k; \boldsymbol{p})$. This fact implies that for any combination of the input parameters $\boldsymbol{p} = (p_1, \dots, p_n)$, the selected path functions return as output the corresponding path signals approximated for that perturbed geometry. Finally, every path functions $\chi_i(k; \boldsymbol{p})$ is weighted for the related $S_{0\,i}^2$ and $\sigma_i^2$ parameters (see eq. (2)) defining the approximated $\chi_i^{\text{approx}}$ contributions. In addition, an energy shift term $\Delta E_{0\,i}$, modifying the values of $k$, can be applied to each new $\chi_i^{\text{approx}}$ term concluding the parametrization phase. A schematic representation of the described methodology is represented in the flow diagram reported in **Figure 1**.
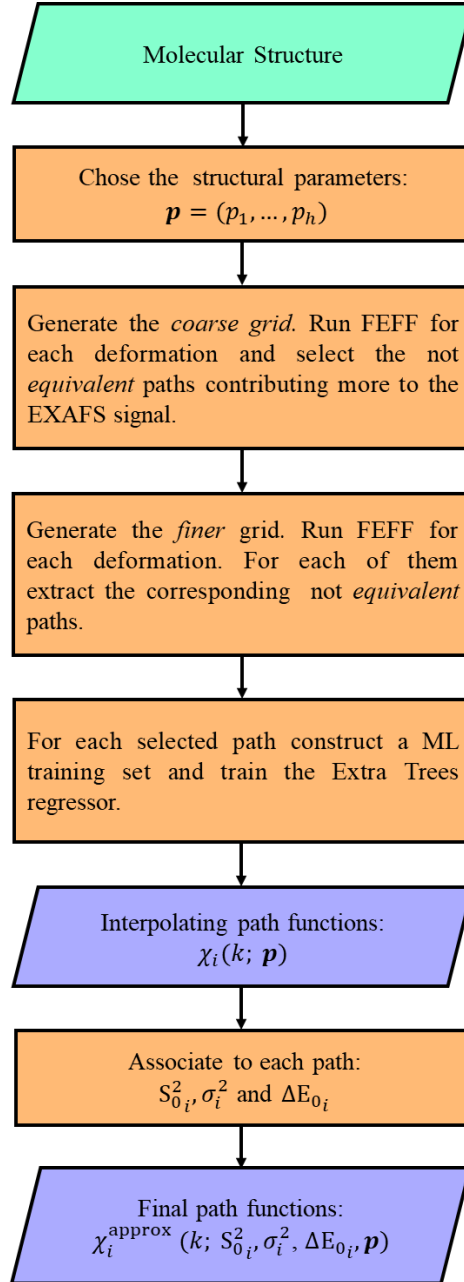
**Figure 1.** Flow diagram reporting the procedure followed to recover the ML-derived path functions $\chi_i$ required to fit an arbitrary experimental EXAFS spectrum.

*2.2. The Fitting Routine*

Once all the $\chi_i^{approx}$ functions are generated, they can be summed together through eq. (1) to obtain the theoretical EXAFS signal $\chi^{THEORY}$, which will be employed in the fitting routine. The fitting parameters are, in this case, $(p_1, ..., p_n)$, common to every $\chi_i^{approx}$ function, and ($S_{0\,i}^2$, $\sigma_i^2$,

$\Delta E_{0_i}$) which can assume different values and parameterizations on the basis of the number and type of atoms involved in the selected paths.

In this work, the fit of the experimental EXAFS signal in the direct ($R$) space was performed minimizing the following $L_2$ norm function:

$$\Xi(R) = \frac{\sum_i \|\Delta\hat{\chi}(R)_i\|^2}{\sum_i \|\hat{\chi}^{DATA}(R)_i\|^2} \qquad (3)$$

Where $\Delta\hat{\chi}(R)$ is the complex residual function defined as: $\Delta\hat{\chi}(R) = \Re[\hat{\chi}^{DATA}(R)_i - \hat{\chi}^{THEORY}(R)_i] + \Im[\hat{\chi}^{DATA}(R)_i - \hat{\chi}^{THEORY}(R)_i]$ while $\|...\|^2$ is the Euclidean norm. The $\hat{\chi}^{DATA}$ and $\hat{\chi}^{THEORY}$ terms represent the Fourier Transform of the experimental and theoretical EXAFS signals weighted for an arbitrary $k^n$ factor.

The minimization of $\Xi$ can be realized employing the standard least squares approach,[32] the simplex method[33] or even a branch of different other techniques, implemented, for example, in the MINUIT CERN library.[34] In the proposed method, since the terms $\chi_i^{approx}$ are non-continuous numerical functions deriving by the Extra Trees approximation, the Powell algorithm,[35,36] not requiring any derivatives of eq. (3), was employed for the minimization routine. The ML-based paths functions return, for any combination of parameters, the corresponding path signal in a lapse of time approximatively immediate. This fact makes the time required for the minimization of the objective ($L_2$ norm) function through this algorithm almost comparable with the one provided by the Artemis code.

The parameters uncertainties can be estimates in various ways. Usually, the main strategy consists in considering the inverse of the Hessian (H) of $\Xi$ evaluated in correspondence of its minimum value. It is possible to demonstrate, in fact, that the diagonal elements of $H^{-1}$ are the squared parameter errors while the off-diagonal elements, when divided by the square root of the product of the corresponding diagonal elements provide the related correlation values.[37,38]

However, this approach may fail when the minimum of eq. (3) is close to a boundary[39] or when the target function $\Xi$ is non-differentiable, as in this case. Herein, we estimated the uncertainties in the form of statistical test recurring to the Fisher (F)-Test.[40] Once a global minimum is found, for each section of $\Xi$, it is possible to vary the related parameter in the neighbor of the minimum and evaluate the region where the Fisher variable increases above a user-defined confidence level (here set to 68 %)[13,41] assuming a number of degree of freedom (D.O.F) equals to: $N_{idp} - \nu$, where $\nu$ is the number of fitting parameters. Further information about this statistical approach can be found in ref.[42,43]

Finally, a more sophisticated fitting procedure involving the Wavelet Transform (WT)[44] representation has also been implemented and tested although not considerable differences emerged using this space of fit. The details of this last fitting procedure are reported in **Section S5** of the S.I., while for sake of completeness the WT fit of the EXAFS spectrum referring to [RuCl$_2$(CO)$_3$]$_2$ has been added to the final part of **Section 3.2**. The entire methodology described in this manuscript was developed in Python using the ML libraries of the PyFitIt code.

## 3. Results and Discussion

*3.1. Case study for KAu(CN)$_2$ complex*

In this section, we present, as a first case study, the ML-based EXAFS analysis of the KAu(CN)$_2$ molecular complex illustrated in the top panel of **Figure 2**. Details concerning the data acquisition techniques are reported in **Section S2** of the S.I. The dicyanoaurate ion Au(CN)$_2^-$ is a tecton, widely employed in solid state chemistry because of the versatility of the intermolecular interactions, consisting in hydrogen-bonds and aurophilic contacts that it can establish.[45-50] In addition, its linear shape favors the formation of supramolecular 1D, 2D, and 3D networks that have demonstrated interesting properties of phosphorescence, vapochromism and giant negative

linear compressibility (GNLC).[48,51-55] The structure is characterized by an approximatively linear geometry.

Starting from the crystallographic Au(CN)$_2^-$ structure,[48] three structural parameters have been selected for the refinement (see **Figure S5**): the two Au–(CN) distances $\Delta d_{Au-(CN)}$, the variation $\Delta\alpha$ of the angles defined by the rotation of the bond axis Au–C$_1$N$_1$ and Au–C$_2$N$_2$, and finally the tilting $\Delta\beta$ of the C$_1$–N$_1$ and C$_2$–N$_2$ bonds. The C–N distances were maintained fixed at the crystallographic values of 1.174 Å. The *coarse* grid associated to these parameters was generated assuming a range of variation for $\Delta d_{Au-(CN)}$ within −0.12 and +0.12, and for $\Delta\alpha$ and $\Delta\beta$ within −15° and +30° respect to the initial structure.

Based on the FEFF calculations, small variations are observed in the amplitudes and phases of the SS paths involving the Au absorber and the C$_1$ and C$_2$ scattering atoms (**Figure 2**abc) as a function of the Au–C bond distances. On the other hand, an abrupt diminution of the amplitude and a non-linear variation of the phase was found for the MS paths Au→C$_1$→C$_2$→Au (or Au→C$_2$→C$_1$→Au) varying the angle α from 180° till to 120° (**Figure 2**def). To select the most relevant paths required for the fitting procedure (see **Section 2.1**), we fixed the rank cutoff at 15%. Under this constraint, the list of the most intense not *equivalent* paths contained the following items: Au→C$_1$→Au (SS), Au→N$_1$→Au (SS), Au→C$_1$→N$_1$→Au (MS with 3 legs), Au→C$_1$→N$_1$→C$_1$→Au (MS with 4 legs) and finally Au→C$_1$→Au→C$_2$→Au (MS with 4 legs).
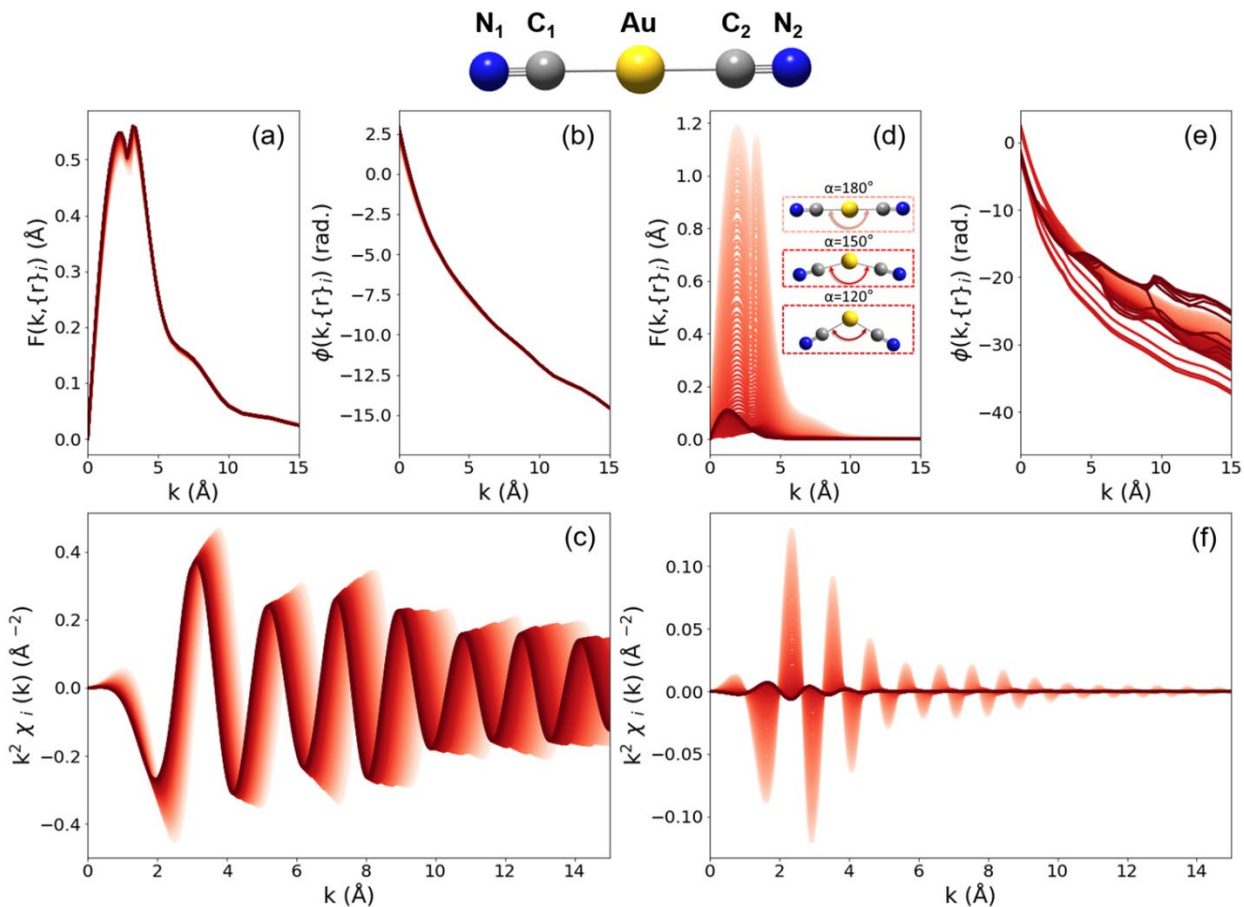
**Figure 2.** Effective scattering amplitudes, phase shifts, and related EXAFS contributions as a function of the deformations involving the $Au(CN)_2$ molecule showed on the top of the figure. Panels (a), (b) and (c) refers to a single scattering process referring to the paths $Au \rightarrow C_1 \rightarrow Au$ or $Au \rightarrow C_2 \rightarrow Au$. The curves have been generated by shifting in parallel the $C_1N_1$ and $C_2N_2$ groups along the bond directions from $-0.12$ Å (light red curve) till to $+0.12$ Å (dark red curve) with respect to the crystallographic structure. Panels (d), (e) and (f) are related to the three legs MS paths: $Au \rightarrow C_1 \rightarrow C_2 \rightarrow Au$ or $Au \rightarrow C_2 \rightarrow C_1 \rightarrow Au$, which change from a collinear configuration ($\alpha = 180°$: light red curve) to a triangular ($\alpha = 120°$: dark red curve). Color code: Au (yellow), N (blue), C (grey).

In general, due to the not absolute symmetry of the CN groups with respect to the Au absorber (in terms of bond distances), we noted that for some perturbed geometry, the FEFF *pathfinder* provides the path $Au \rightarrow C_2 \rightarrow Au$ with degeneration 2 instead of $Au \rightarrow C_1 \rightarrow Au$. Independently of the atom enumeration, these paths were considered under the same typology: $Au \rightarrow C_1 \rightarrow Au$. This approach was extended also to every relevant MS path in case of disagreement with the ones indicated in the not *equivalent* paths list. The *finer* grid in the space of structural parameters was

built varying the quantities $\Delta d_{\text{Au-(CN)}}$, $\Delta\alpha$ and $\Delta\beta$ for 500 times following the IHS scheme. Afterwards, for each selected deformation, the related input structure was generated and the FEFF routine was executed.

In case of two (or more) *equivalent* paths for the same molecular deformation, for example Au→C$_1$→Au and Au→C$_2$→Au with degeneration 1, both the signals were extracted, summed and saved in the corresponding dataset named, in this case Au→C$_1$→Au. This approach can be clearly followed, if and only if, it is supposed that both the paths are characterized by the same DW parameter. If this condition is not satisfied (not considered in this example) the Au→C$_2$→Au must be decoupled from the Au→C$_1$→Au path and considered as a separate contribution.

At the end of the selection procedure, five training datasets (Au→C$_1$→Au, Au→N$_1$→Au, Au→C$_1$→N$_1$→Au, Au→C$_1$→N$_1$→C$_1$→Au and Au→C$_1$→Au→C$_2$→Au), were employed to train the regressor algorithm. The quality of prediction associated to each non-linear path function was obtained recurring to the ten-folded cross-validation (CV) technique.[25] The CV results, reported in **Table S1**, indicate also here an optimal reproducibility for each not *equivalent* path supposed to characterize the complex. The DW factors associated to the SS paths: Au→C$_1$→Au and Au→N$_1$→Au, were defined using the quantities $\sigma_C$ and $\sigma_N$. On the other hand, the MS DW terms were parametrized as: $\sigma_{MS}^2 = \sqrt{\sum_i \sigma_i^2}$, where $\sigma_i^2$ are the DW factors of the atoms involved in the scattering process. The latter constitutes the unique parameterization required by this method. For all the scattering paths, common $S_0^2$ and $\Delta E_0$ were assumed.

The fit of the EXAFS spectrum was carried out in *R*-space range from 1 up to 4 Å, assuming a *k*-space range for the Fourier Transform within 2.6 and 12 Å$^{-1}$, resulting in the number of independent points $N_{\text{idp}} \approx 18$. Seven fitting parameters were employed in the refinement: $\Delta d$, $\Delta\alpha$, $\Delta\beta$, $\sigma_C$, $\sigma_N$, $S_0^2$ and $\Delta E$. The EXAFS fit was realized inside their related range of variation. Besides

the $\Delta d_{Au\text{-}(CN)}$, $\Delta\alpha$ and $\Delta\beta$ described above, the following further bounds were considered: $\sigma_C$ and

$\sigma_N \in (0.001 \div 0.015)$ $\text{Å}^2$, $S_0^2 \in (0.8 \div 1.3)$, $\Delta E_0 \in (-10 \div 10)$ eV. The result of the

minimization of eq. 3 is summarized in **Table 1** together with the parameters confidence intervals,

while the comparison between the experimental and best-fit FT EXAFS representation is reported

in **Figure 3**. The fit of the EXAFS spectrum employing the WT representation is showed in

**Section S5.1** of the S.I. The best-fit results obtained with this approach have been further verified

through an EXAFS fit realized using the Artemis software. Herein the refined parameters were

used to generate the corresponding $KAu(CN)_2$ structure that has been employed in the least-

squares optimization of **Section S6.1** of the S.I text. The latter shows the same %R-factor (*vide*

*infra*) identical to the one found by our approach, and the deviations from the ML-refined

parameters are comparable to zero.

**Table 1**. Best Fit Parameters ($L_2$ minimization output) obtained minimizing the target function of eq. (3) considering the set of deformations shown in **Figure S5**. The uncertainties reported in the last column were obtained through the F-test fixing a confidence level of 68% for 11 D.O.F.

| Best Fit Parameters | | Confidence Intervals |
|---|---|---|
| $S_0^2$ | 0.91 | $0.8 \div 1.04$ |
| $\Delta E_0$ (eV) | 7.92 | $6.38 \div 9.71$ |
| $\sigma_C$ (Å$^2$) | 0.0024 | $0.001 \div 0.005$ |
| $\sigma_N$ (Å$^2$) | 0.001 | $0.001 \div 0.004$ |
| $\Delta d_{\text{Au-(CN)}}$ (Å) | -0.01 | $-0.03 \div 0.01$ |
| $\alpha$ (°) | 168.88 | $138.84 \div 210$ |
| $\beta$ (°) | $-1.32$ | $-15 \div 11.42$ |
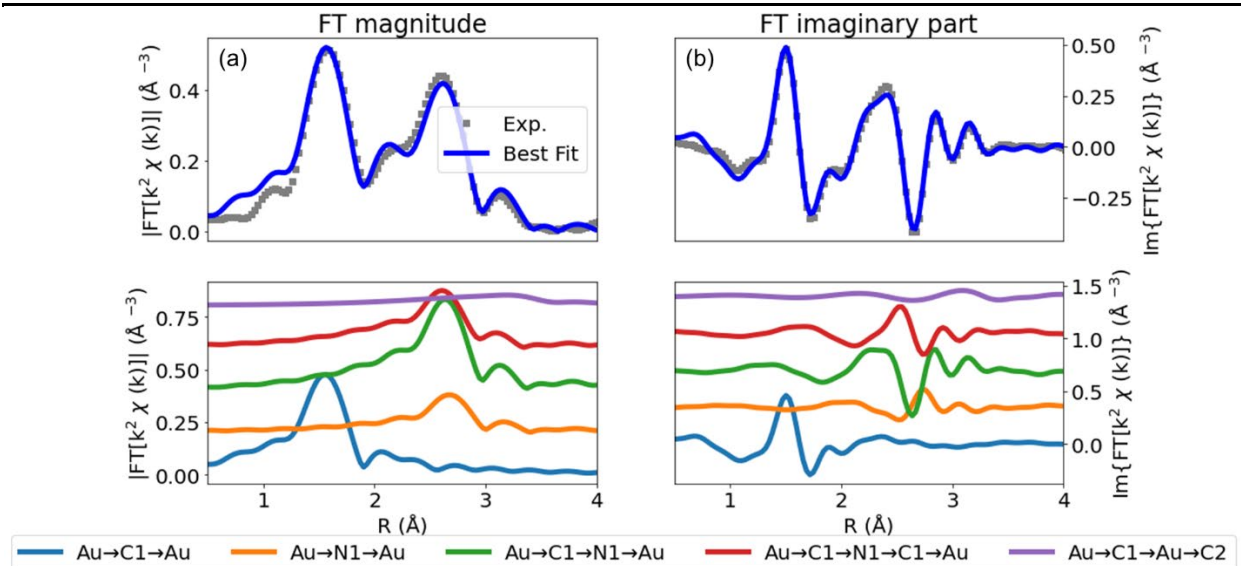


**Figure 3.** Phase uncorrected (a) modulus and (b) imaginary part of the experimental and best-fit FT EXAFS spectra for the KAu(CN)$_2$ complex. The experimental data are showed as grey squares while the best-fits with blue solid lines. The principal SS and MS contributions included in the fitting model are reported in the bottom panels as colored solid lines, vertically translated for sake of the clarity.

**Figure 3** demonstrates that all the main spectral features, due to SS and MS effects, appearing in the experimental FT-EXAFS spectrum are properly reproduced by the best fit curve. The %R-factor (IXS)[56] associated to the fit, is found to be equal to 1.3%, demonstrating that the theoretical representation is in good agreement with experiment. The small misfit between the theoretical and

the experimental EXAFS curves, particularly visible in the resulting FT-magnitude in **Figure 3**a at ca. 2.5 – 2.75 Å, are attributed to low intensity SS and MS contributions due to the presence of water molecules surrounding the gold complex, neglected in this example.

The $\Delta d_{Au\text{-}(CN)}$ quantity is refined to $-0.0l$ Å, which is a negligible contraction of the CN groups from the Au absorber, in line with the crystallographic model. The variation of $\Delta\alpha$ from the initial configuration it is not found to be equal to $0°$ (i.e. $\alpha = 180°$) but of ca. $5.57°$ (i.e. $\alpha \approx 169°$). However, the uncertainty associated to the estimation of this parameter is quite large. Thanks to the ML-based approach, it is possible to analyze in fact the $\Delta\alpha$ dependence of the $\Xi$ section, as showed in **FigureS6**a. It is evident that the $\Xi$ function shows a weak variation as a function of $\Delta\alpha$. In particular, the $\Xi$ trend does not possess a proper unique minimum but a flat line extending within ca. $\pm7.2°$ ($\alpha \approx 194.4°$) and ($\alpha \approx 165.6°$). Furthermore, it is worth noting that the Au→$C_1$→Au→$C_2$→Au path is the only EXAFS contribution possessing a connection with the $\Delta\alpha$ variation. If compared with all the other not *equivalent* scattering processes affecting the total EXAFS signal, it possesses always the lowest rank intensity for every kind of selected deformation as showed in **Section S3.3**. This fact causes that the influence of $\Delta\alpha$ on $\Xi$ is overpowered by the other parameters involved in the refinement, see **Figure 4**a. Despite this fact, the exclusion of the Au→$C_1$→Au→$C_2$→Au path from the fitting procedure causes an increase of the %R-factor to ca 2.4%, indicating the necessity of its employment.

Most of the confidence intervals for the fitted parameters, showed in **Table 2**, are not symmetric. This evidence is principally due to the employment of boundaries regions during the minimization routine. An interesting result is represented by the DW value for the SS Au→N path, which coincides with the lowest boundary of the $\sigma_N$ range of variation. This result can be understood considering that the DW factor is a measure of the mean-square displacement of the atoms from

their equilibrium position. In the analyzed example, each N atom is connected to a C atom through a triple bond avoiding its independent variation, justifying this finding.

Considering the $\Delta\beta$ parameter (connected to the Au→$C_1$→$N_1$→Au and Au→$C_1$→$N_1$→$C_1$→Au MS paths), its variation, is assessed to be ca. $-1.3°$. However, as for the precedent case, the related confidence interval suggests this value is comparable with the null variation of $\Delta\beta$. In particular, $\Xi$ shows a negligible variation for the $\beta$ values within ca. $-6.3°$ and $6.3°$, as showed in **FigureS6**b. Below and above these two quantities the changings of $\Xi$ are more intense than for the $\alpha$ case determining a narrower uncertainty range. This fact is also evident analyzing the contour plot of $\Xi$ evaluated for $\Delta d$ and $\Delta\beta$, see **Figure 4**b, where a more localized valley can be clearly identified.

Summarizing this first case study, we demonstrated that it is possible to obtain a detailed description of the bond distances through the EXAFS fitting procedure, validating the initial unperturbed model. Moreover, the ML approach allowed to investigate the angular dependence of the principal MS paths emerging from the selected structure. Herein, we have showed that these contributions are approximatively stable for small variations of the related $\alpha$ and $\beta$ angles around the initial (linear) structure determining an enlargement of the uncertainty associated to their estimation through the EXAFS fitting procedure, while for their larger perturbations, stronger changes in $\Xi$ appear connected to an abrupt diminution of the reproduction of the experimental spectrum using the theoretical one.
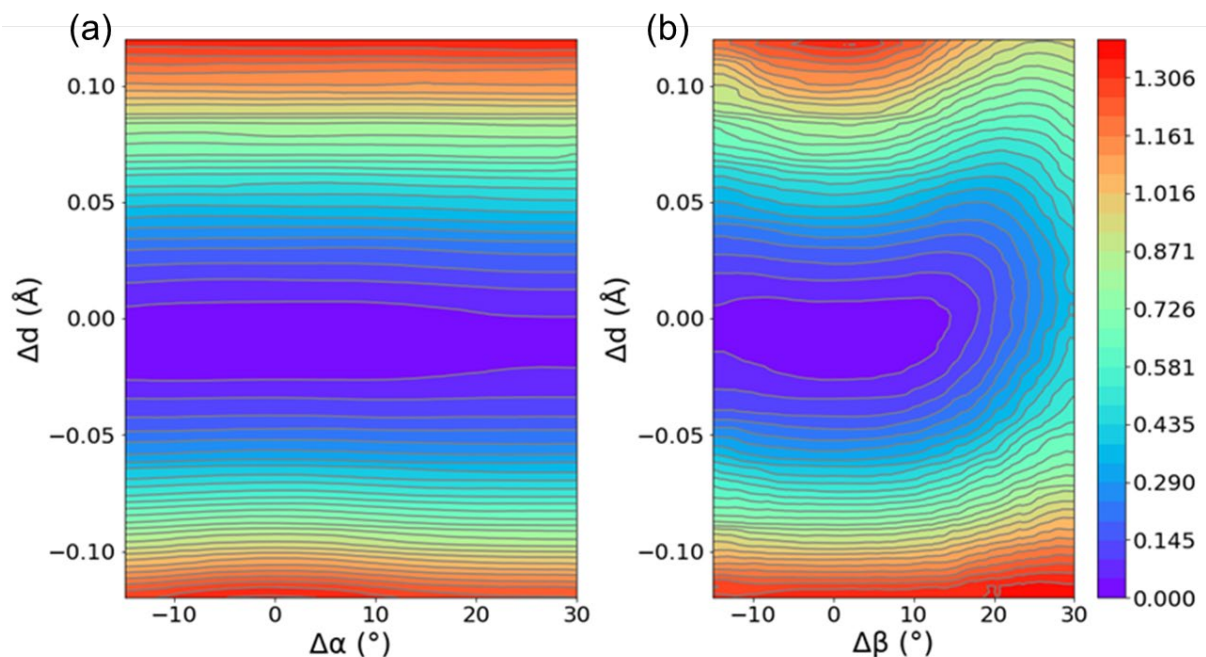
**Figure 4.** Contour plot map of Ξ obtained varying Δd and Δα maintaining all the remaining parameters fixed to the best fit values. (b) The same as (a) but varying Δβ.

*3.2. Case study for the [RuCl$_2$(CO)$_3$]$_2$ complex*

Halogenocarbonylruthenium complexes have a range of promising catalytic[57,58] and biomedical[58-60] applications. In this section, we analyze the EXAFS data of the [RuCl$_2$(CO)$_3$]$_2$ complex, in which the so-called forward MS paths have a strong dependence on the position of the intermediate scatterer (*vide infra*). The experimental details and data collection were recently reported by De Vos and coworkers.[58] Since the Ru–Ru contribution is negligible, the binuclear structure of [RuCl$_2$(CO)$_3$]$_2$ was approximated by a mononuclear RuCl$_3$(CO)$_3$ model (molecular structure showed in **Figure 5**a). Without changing the angle with respect to the initial D$_{4h}$ symmetry, only the three interatomic distances, Ru–O ($\Delta d_O$), Ru–C ($\Delta d_C$), and Ru–Cl ($\Delta d_{Cl}$) were varied (see **Figure S8**) within the −0.12 – 0.12 Å range with respect to the starting geometry. With a rank cutoff set to 15%, the following paths were selected: Ru→C$_1$→Ru (SS), Ru→O$_1$→Ru (SS), Ru→Cl$_1$→Ru (SS), Ru→O$_1$→C$_1$→Ru (MS with 3 legs) and finally Ru→C$_1$→O$_1$→C$_1$→Ru (MS

with 4 legs). It is important to note that for the single forward (Ru→C→O→Ru) and double forward (Ru→C→O→C→Ru) MS paths, a strong dependence of the scattering amplitude on the position of the intermediate C atom is observed even if the total path length (i.e. Ru–O distance) is fixed, as demonstrated in **Figure 5**. This fact significantly influences the fit quality within a classical procedure as demonstrated in **Section 3.3**.
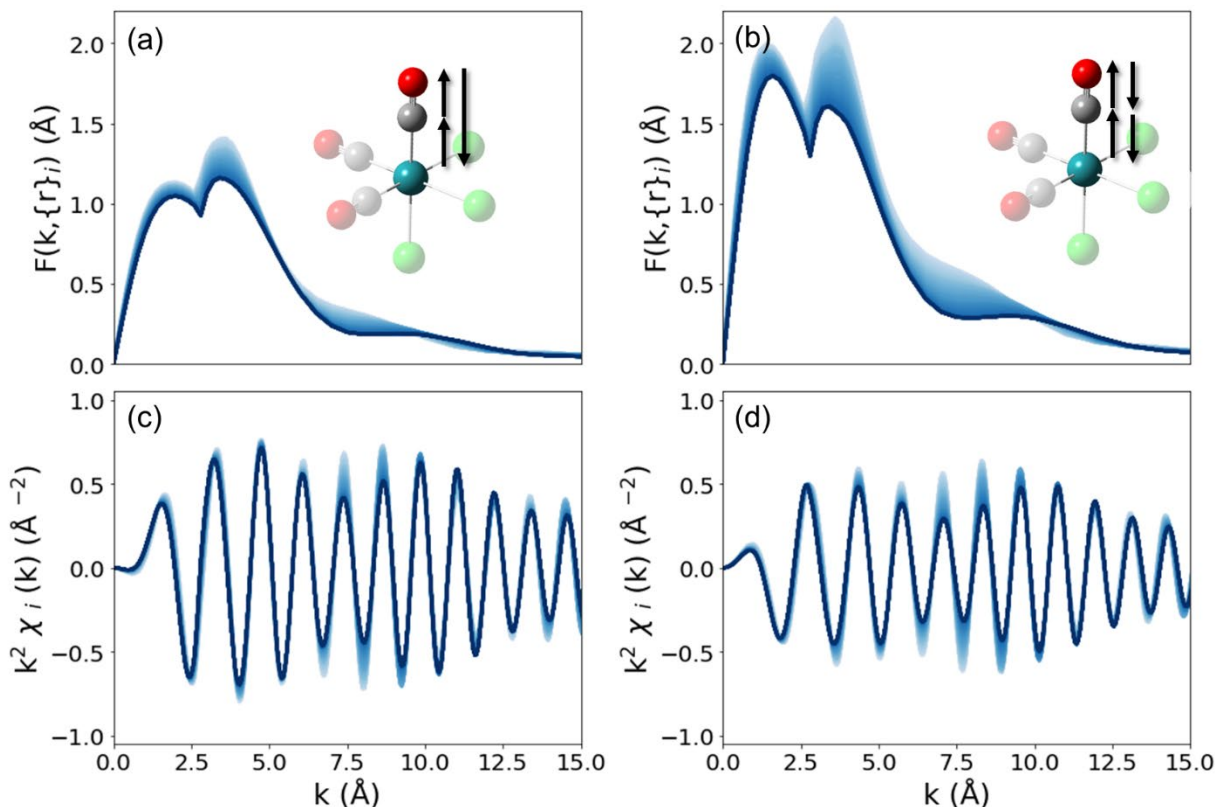


**Figure 5.** Trend of the backscattering amplitudes (on the top) and of the related EXAFS path function (on the bottom) referring to the Ru→$C_1$→$O_1$→Ru (a, c) and Ru→$C_1$→$O_1$→$C_1$→Ru (b, d) scattering process showed in the insets, respectively. The curves have been obtained keeping fixed the Ru-O distance at 3 Å and varying the Ru–C bond length from 1.78 Å (light blue) till to 2.2 Å (dark blue). Color code: Ru (blue), Cl (green), O (red), C (grey).

As in the previous example, the *finer* grid was built varying the Ru–O, Ru–C, and Ru–Cl distances 500 times following the IHS scheme and selecting all not *equivalent* paths after the FEFF routine. The 10-fold CV results, reported in **Table S2**, indicate an optimal reproducibility for each selected not *equivalent* path.

The five non-linear paths functions were then weighted for their related DW factors. The DW factors associated to the SS paths: Ru→$C_1$→Ru, Ru→$O_1$→Ru and Ru→$Cl_1$→Ru were defined using the related quantities: $\sigma_C$, $\sigma_O$ and $\sigma_{Cl}$. On the other hand, the MS DW terms have been parametrized with the same $\sigma_O$ term. For all the paths, the variables $S_0^2$ and $\Delta E_0$ were assumed common. The theoretical and experimental EXAFS signals were Fourier transformed in the 4-16 $\text{Å}^{-1}$ range while the fit was performed in $R$ range from 1 to 3 Å ($N_{\mathrm{idp}} \approx 15$). The target function showed in eq. (3) is characterized, in this case, by eight fitting parameters: Ru–O, Ru–C, and Ru–Cl distances, $\sigma_C$, $\sigma_O$, and $\sigma_{Cl}$, $S_0^2$ and $\Delta E_0$, with the boundary conditions $\sigma \in (0.001 \div 0.01)$ $\text{Å}^2$ for all DW factors, $S_0^2 \in (0.8 \div 1.3)$ and $\Delta E_0 \in (-10 \div 10)$ eV. The fit results are shown in **Table 2** together with the parameters confidence intervals. The best-fit FT EXAFS curves are reported in **Figure 6**. The %R-factor (IXS)[56] is 0.9 %, demonstrating that the theoretical representation is in good agreement with the experiment in the selected range of fit. Similarly, to what has been done in **Section 3.1**, we reinforced our finding fitting with the Artemis the ML-refined structure; see **Section S6.2** of the S.I. Also, for this case study, the deviations of the structural parameters from the ML-refined ones are close to zero, and the %R-factor remains stable to 0.9%, underlying the goodness of our results.
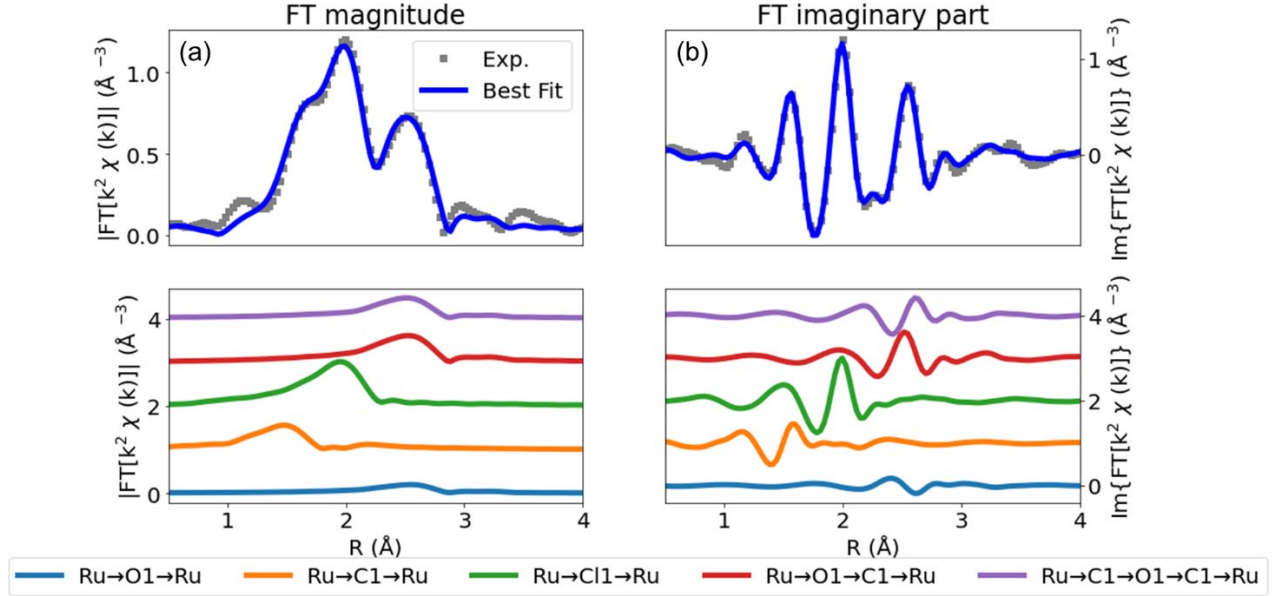
**Figure 6.** Phase uncorrected (a) modulus and (b) imaginary part of the experimental and best-fit FT EXAFS spectra for $RuCl_2(CO)_3$. The experimental data are showed as grey squares while the best-fits with blue solid lines. The principal SS and MS contributions included in the fitting model are reported in the bottom panels as colored solid lines, vertically translated for sake of the clarity.

**Table 2.** Best Fit parameters ($L_2$ minimization output) obtained minimizing the target function of eq. (3) considering the set of deformations reported in **Figure S9**. On the right columns are indicated the parameters uncertainties obtained through the F-test approach fixing a confidence level of 68% for 7 D.O.F.

| Best Fit Parameters | | Confidence Intervals |
|---|---|---|
| $S_0^2$ | 1.21 | $0.93 \div 1.3$ |
| $\Delta E_0$ (eV) | $-2.06$ | $-5.68 \div 1.07$ |
| $\sigma_C$ (Å$^2$) | 0.004 | $0.0015 \div 0.008$ |
| $\sigma_O$ (Å$^2$) | 0.0055 | $0.0029 \div 0.009$ |
| $\sigma_{Cl}$ (Å$^2$) | 0.0048 | $0.0027 \div 0.0075$ |
| Ru–C (Å) | 1.91 | $1.89 \div 1.94$ |
| Ru–O (Å) | 3.034 | $3.003 \div 3.067$ |
| Ru–Cl (Å) | 2.41 | $2.38 \div 2.43$ |

As a proof of concept of the results obtained through the classical FT EXAFS fit, we show, in the

following, also the refinement of the above structure employing the WT representation. Details

concerning the target function definition are reported in **Section S5** of S.I. The comparison between the theoretical and experimental WT 2D map is reported in **Figure 7**, while the best-fit parameters obtained though the WT refinement are indicated in **Table 3**. As it is possible to see from the comparison, all the main WT features of the experimental spectrum are properly reproduced by the theoretical WT representation. The R-factor associated to the fit is found to be equal to the one proper of the FT-based fit, while the confidence intervals, evaluated for each parameter involved in the fit are close to the ones showed in **Table 2**.

Summarizing this case study, it is important to note, that an example with the strong dependence of the SS paths on the position of the intermediate atoms was considered and the advantage of the developed ML-based fit of EXAFS over classical fit was demonstrated.
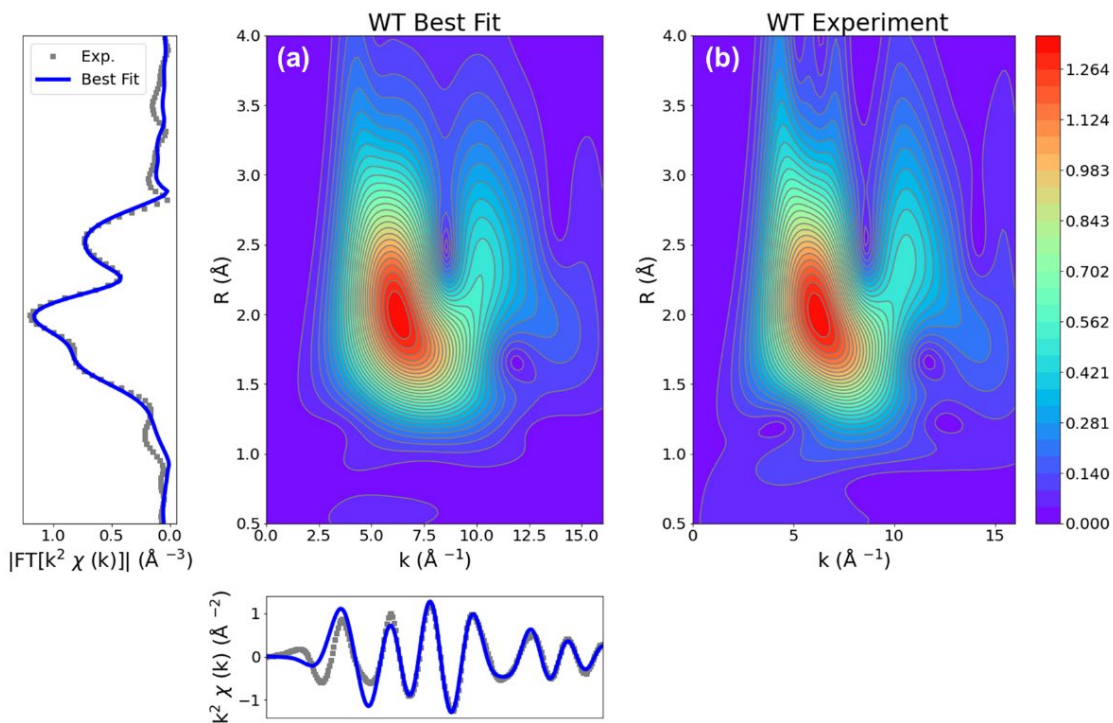


**Figure 7:** Plot of the EXAFS best-fit WT representation (phase uncorrected). The bottom and left panels report the comparison between the best-fit EXAFS curve, evaluated using the parameters found to minimize eq. (S.3), and the experimental spectrum plotted in the $k$ and $R$ (phase-uncorrected) spaces. The fit has been realized in the $\Delta k \times \Delta R = (0 - 16)$ Å$^{-1}$ $\times (1 - 3)$ Å 2D grid assuming a Hanning apodization window

defined within 4 and 16 Å$^{-1}$. (b) WT representation of the experimental EXAFS signal. For both the WT representations, the same mother wavelet resolution parameters have been employed: $s = 1$ and $\eta = 5$.

**Table 3:**Best Fit Parameters (L$_2$ minimization output) obtained from the WT representation, minimizing the target function of eq. (S.4) considering the set of deformations reported in **Figure S9**(a, b, c). On the right columns are indicated the parameters uncertainties obtained through the F-test approach fixing a confidence level of 68% for 7 D.O.F.

| Best Fit Parameters | | Confidence Intervals |
|---|---|---|
| $S_0^2$ | 1.21 | $0.94 \div 1.3$ |
| $\Delta E$ (eV) | $-1.93$ | $-5.60 \div 1.48$ |
| $\sigma_C$ (Å$^2$) | 0.004 | $0.0018 \div 0.008$ |
| $\sigma_O$ (Å$^2$) | 0.0055 | $0.0029 \div 0.01$ |
| $\sigma_{Cl}$ (Å$^2$) | 0.0048 | $0.0028 \div 0.0075$ |
| Ru–C (Å) | 1.9 | $1.88 \div 1.93$ |
| Ru–O (Å) | 3.036 | $3.01 \div 3.07$ |
| Ru–Cl (Å) | 2.405 | $2.38 \div 2.43$ |

*3.3. Fit of the [RuCl₂(CO)₃]₂ complex using the classic EXAFS fit: when the initial geometry makes the difference*

As demonstrated in **Figure 5**, two MS paths which provide a strong contribution to the EXAFS signal have a strong dependency on the input geometry. Below, the standard EXAFS fitting using Artemis software was performed.
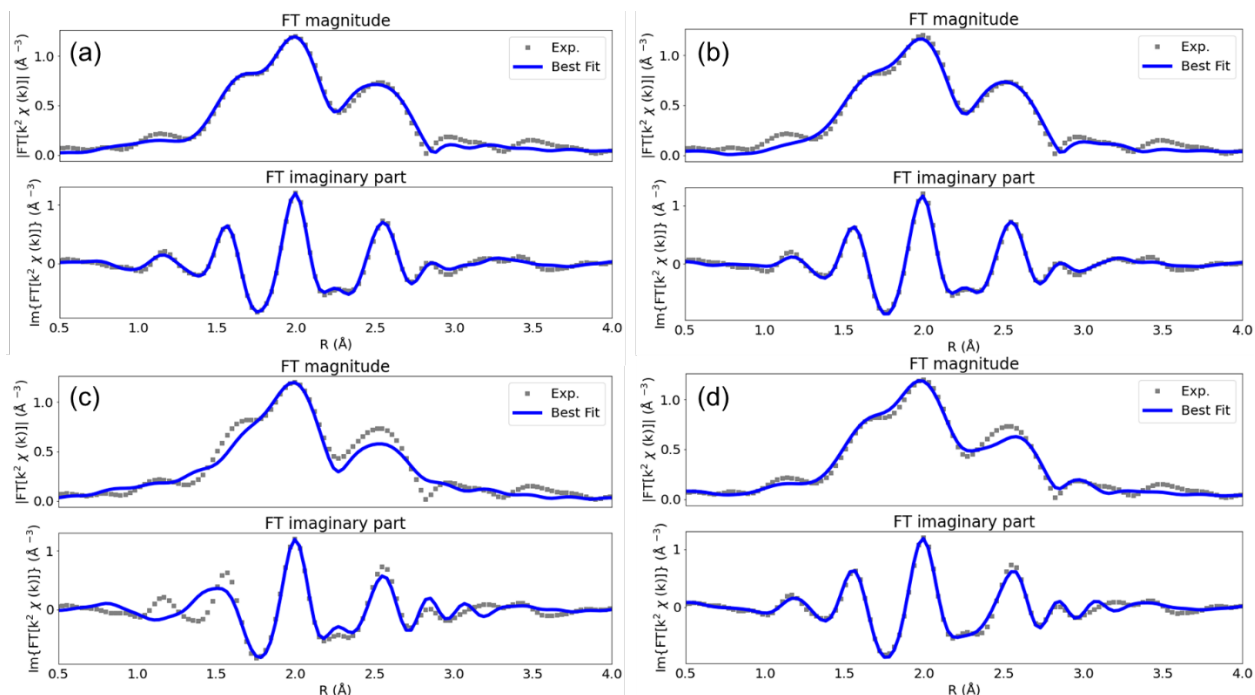
**Figure 8:** Fit of the experimental EXAFS signal obtained using the Ru(CO)$_3$Cl$_3$ model starting from different values of the Ru–C distance and with a common Ru-O bond length set to 3.0 Å. (a) Ru–C distance of 1.70 Å, corresponding to the minimal contraction of the Ru–C bond ($\Delta d_C = -0.2$ Å) (b) Ru–C distance of 1.90 Å. (c) Ru–C distance set to 2.2 Å ($\Delta d_C = +0.2$ Å). (d) Fit of the EXAFS signal based on the model with the Ru–C bond distance set to 2.2 Å but employing the Ru–C path generated for the Ru–C distance of 1.90 Å.

First, the initial geometry was characterized by Ru−C and Ru−O distances of 1.70 and 3.0 Å, respectively. The fit, reported in **Figure 8**a, using $k^2$-weighted data in the $4-16$ Å$^{-1}$ range results in %R-factor of ca 0.7%. The fitted $R_{Ru-C}$ is $1.90 \pm 0.01$ Å while the $R_{Ru-O}$ is found to be equal to $3.04 \pm 0.01$Å.

How it is possible to see, the %R-factor is slightly lower than the one obtained using the ML-fitting approach, however it is possible to demonstrate easily that the fitting result obtained by the Artemis code appears to depend on the input geometry, allowing to accommodate just small variation of distances starting from the guessed structure. This fit requires, in fact, a considerable shift of the Ru-C distance from 1.70 Å to the best-fit value of 1.90 Å. Correcting the RuCl$_3$(CO)$_3$ structure on the basis of this result and performing again the fit, it is possible to observe that the

Ru–C distance is refined by the least squares approach[32] with a negligible variation of $\Delta d_C =$ 0.004 $\pm$ 0.006 Å, see **Figure 8**b. However, in this case, the %R-factor is increased to 0.9%, similarly to what it has been found through the fitting procedure described in the precedent section. The reason of the discrepancy between the two approaches must be found in the molecular geometry dependence of the amplitudes and of phases of the SS and MS paths generated by the code, which are calculated, through an *ab initio* approach, just one time for the structure with a Ru–C bond length of 1.70 Å. The these curves are remain in fact unaltered for the extension of the Ru–C bond to $\Delta d_C = +0.20$ Å, as already critically noticed by Ravel.[29] This approximation is instead not applied in our method, where each selected path is numerically approximated for the continuous variations of the geometric parameters, providing a more accurate refinement of the structure.

If the starting Ru–C is increased to 2.2 Å keeping Ru–O distance unchanged, the related R-factor increases to 13% (see **Figure 8**c). The fitted $R_{Ru-C}$ is optimized to 2.36 $\pm$ 0.07 Å, which is clearly unphysically large, indicating how the Artemis code, using the amplitudes and phases generated starting from the structure with a Ru–C=2.2 Å is not able to fit properly the experimental spectrum. Herein, the geometry dependence of the paths can be further underlined involving in a fourth refinement this structure (Ru–C of 2.2 Å) but taking the independent Ru–C path from the second structure ($R_{Ru-C}$ = 1.90 Å) and assigning to it an independent $\Delta E_0$. This fit, reported in **Figure 8**d employs one parameter more than the ones reported before and it appears characterized by an R-factor of 1.2% for a Ru-C distance of 1.88 $\pm$ 0.02 Å. This quantity is higher than the one realized with the model initialized with a Ru-C=1.9 Å and the difference is attributable to the MS contributions.

Concluding, these examples demonstrate how the choice of the starting geometry affect not only the values of the fitted parameters but also the overall fitting quality, showing, unambiguously, that finding the best fit is not a trivial task, especially when MS paths are involved. In this representative example, the developed ML approach appears to be highly beneficial.

## 4. Conclusions

We have developed a novel fitting approach based on ML that aims to improve the classic multiple scattering EXAFS fit methodology. This approach allows one to overcome the known issue, proper of the standard EXAFS fitting procedure, related to the dependency of the theoretical phases, amplitudes and electron mean free paths from the input geometry, which has been shown to be a critical aspect for multiple scattering process. Unlike other fitting approaches, the proposed methodology allows optimizing the parameters directly describing the 3D geometry without the requirement of any complex parametrization, leading to a strong simplification in the EXAFS analysis. We have demonstrated the validity and advantages of this novel approach fitting the EXAFS data for representative Au- and Ru-based molecular complexes.

## Author Information

**Corresponding Authors (*)**

A. Martini: andrea.martini@unito.it; A. L. Bugaev: abugaev@sfedu.ru.

## Supporting Information

**Part S1**. Fitting routine: Multidimensional *coarse* grid plot (**Figure S1**); Equivalence criterion scheme (**Figure S2**); Plot of the IHS points distributions (**Figure S3**); KAu(CN)$_2$ paths datasets (**Figure S4**). **Part S2**. Experimental data. **Part S3**. EXAFS analysis of the KAu(CN)$_2$ spectrum: Set of deformations employed in the fit of the KAu(CN)$_2$ complex (**Section S3.1**, **Figure S5**); Quality of prediction associated to each ML path function (KAu(CN)$_2$ complex case) (**Section 3.2**, **Table S1**); Curve wave amplitude analysis of the main MS processes for the KAu(CN)$_2$ case (**Section S3.3**, **Figure S6** and **Figure S7**); Error curves evaluated for the variation of the α and β parameters around the minimum found by the refinement (**Section S3.4** and **Figure S8**).

**Part S4**. EXAFS analysis of [RuCl$_2$(CO)$_3$]$_2$ complex: Set of deformations employed in the fit of the [RuCl$_2$(CO)$_3$]$_2$ complex (**Figure S9**); Quality of prediction associated to each ML path function (the [RuCl$_2$(CO)$_3$]$_2$ complex case) (**Table S2**). **Part S5**. EXAFS wavelet transform fitting routine description: EXAFS Wavelet Transform fit of the KAu(CN)$_2$ complex (**Section 5.1**, **Table S3** and **Figure S10**). **Part 6**. Validation of the ML-refined structures through the classic EXAFS

fitting procedure: KAu(CN)$_2$ case (**Section S6.1**, **Figure S11** and **Table S4**); [RuCl$_2$(CO)$_3$]$_2$ case

(**Section 6.2**, **Figure S12** and **Table S5**).

## Abbreviations

EXAFS, Extended X-ray Absorption Fine Structure. SS, single scattering. MS, multiple scattering.

DW, Debye Waller. ML, Machine Learning. FT, Fourier Transform. WT, Wavelet Transform,

WT. D.O.F. Degree of freedom. CV, Cross Validation.

## References

(1)     Rehr, J. J.; Albers, R. C. *Rev. Mod. Phys.* **2000**, *72*, 621.
(2)     Van Bokhoven, J. A.; Lamberti, C. *X-ray absorption and X-ray emission spectroscopy: theory and applications*; John Wiley & Sons, 2016; Vol. 1.
(3)     Sayers, D. E.; Stern, E. A.; Lytle, F. W. *Phys. Rev. Lett.* **1971**, *27*, 1204.
(4)     Seah, M. P.; Dench, W. A. *Surface and Interface Analysis* **1979**, *1*, 2.
(5)     Frenkel, A. I.; Stern, E. A.; Qian, M.; Newville, M. *Physical Review B* **1993**, *48*, 12449.
(6)     Ravel, B.; Newville, M. *J. Synchrot. Radiat.* **2005**, *12*, 537.
(7)     Zabinsky, S. I.; Rehr, J. J.; Ankudinov, A.; Albers, R. C.; Eller, M. J. *Physical Review B* **1995**, *52*, 2995.
(8)     Lee, P. A.; Pendry, J. B. *Physical Review B* **1975**, *11*, 2795.
(9)     Frenkel, A.; Stern, E. A.; Voronel, A.; Qian, M.; Newville, M. *Phys. Rev. Lett.* **1993**, *71*, 3485.
(10)     Frenkel, A.; Stern, E. A.; Voronel, A.; Qian, M.; Newville, M. *Physical Review B* **1994**, *49*, 11662.
(11)     Frenkel, A.; Voronel, A.; Katzir, A.; Newville, M.; Stern, E. A. *Physica B* **1995**, *208*, 334.
(12)     Frenkel, A. I.; Stern, E. A.; Voronel, A.; Heald, S. M. *Solid State Commun.* **1996**, *99*, 67.
(13)     Filipponi, A.; DiCicco, A. *Physical Review B* **1995**, *52*, 15135.
(14)     Filipponi, A.; DiCicco, A.; Natoli, C. R. *Physical Review B* **1995**, *52*, 15122.
(15)     Dangelo, P.; Dinola, A.; Filipponi, A.; Pavel, N. V.; Roccatano, D. *J. Chem. Phys.* **1994**, *100*, 985.
(16)     D'Angelo, P.; Barone, V.; Chillemi, G.; Sanna, N.; Meyer-Klaucke, W.; Pavel, N. V. *Journal of the American Chemical Society* **2002**, *124*, 1958.
(17)     Kuzmin, A.; Evarestov, R. A. *J. Phys.-Condes. Matter* **2009**, *21*.
(18)     Di Cicco, A.; Trapananti, A.; Faggioni, S.; Filipponi, A. *Phys. Rev. Lett.* **2003**, *91*, 4.
(19)     Timoshenko, J.; Kuzmin, A.; Purans, J. *Comput. Phys. Commun.* **2012**, *183*, 1237.
(20)     Calvin, S. *XAFS for Everyone*, 2013.
(21)     Vlaic, G.; Olivi, L. *Croat. Chem. Acta* **2004**, *77*, 427.
(22)     Hudson, E. A.; Allen, P. G.; Terminello, L. J.; Denecke, M. A.; Reich, T. *Physical Review B* **1996**, *54*, 156.
(23)     Timoshenko, J.; Anspoks, A.; Cintins, A.; Kuzmin, A.; Purans, J.; Frenkel, A. I. *Phys. Rev. Lett.* **2018**, *120*, 6.

(24)     Timoshenko, J.; Wrasman, C. J.; Luneau, M.; Shirman, T.; Cargnello, M.; Bare, S. R.; Aizenberg, J.; Friend, C. M.; Frenkel, A. I. *Nano Lett.* **2019**, *19*, 520.

(25)     Guda, A. A.; Guda, S. A.; Lomachenko, K. A.; Soldatov, M. A.; Pankin, I. A.; Soldatov, A. V.; Braglia, L.; Bugaev, A. L.; Martini, A.; Signorile, M. *Catalysis Today* **2019**, *336*, 3.

(26)     Smolentsev, G.; Soldatov, A. *J. Synchrot. Radiat.* **2006**, *13*, 19.

(27)     Martini, A.; Guda, S.; Guda, A.; Smolentsev, G.; Algasov, A.; Usoltsev, O.; Soldatov, M. A.; Bugaev, A.; Rusalev, Y.; Lamberti, C. *Comput. Phys. Commun.* **2020**, *250*, 107064.

(28)     Guda, A.; Guda, S.; Martini, A.; Bugaev, A.; Soldatov, M.; Soldatov, A.; Lamberti, C. *Radiat. Phys. Chem.* **2020**, *175*, 108430.

(29)     Ravel, B. In *14th International Conference on X-Ray Absorption Fine Structure*; DiCicco, A., Filipponi, A., Eds.; Iop Publishing Ltd: Bristol, 2009; Vol. 190.

(30)     Ravel, B. In *X-Ray Absorption and X-Ray Emission Spectroscopy*; Van Bokhoven, J. A., Lamberti, C., Eds.; Wiley Online Books: 2016; Vol. X-Ray Absorption and X-Ray Emission Spectroscopy, p 281.

(31)     Beachkofski, B.; Grandhi, R. In *43rd AIAA/ASME/ASCE/AHS/ASC Structures, Structural Dynamics, and Materials Conference*.

(32)     Moré, J. J. In *Numerical Analysis*; Watson, G. A., Ed.; Springer Berlin Heidelberg: Berlin, Heidelberg, 1978, p 105.

(33)     Nelder, J. A.; Mead, R. *The Computer Journal* **1965**, *7*, 308.

(34)     James, F.; Roos, M. *Comput. Phys. Commun.* **1975**, *10*, 343.

(35)     Powell, M. J. D. *The Computer Journal* **1964**, *7*, 155.

(36)     Press, W. H.; Teukolsky, S. A.; Vetterling, W. T.; Flannery, B. P. *Numerical recipes in C (2nd ed.): the art of scientific computing*; Cambridge University Press, 1992.

(37)     Bunker, G. *Introduction to XAFS: A Practical Guide to X-ray Absorption Fine Structure Spectroscopy*; Cambridge University Press: Cambridge, 2010.

(38)     Kuzmin, A. *Physica B* **1995**, *208*, 175.

(39)     Newville, M., Stensitzki, Till, Allen, Daniel B., & Ingargiola, Antonino. *Zenodo* **2014**.

(40)     Joyner, R. W.; Martin, K. J.; Meehan, P. *Journal of Physics C-Solid State Physics* **1987**, *20*, 4005.

(41)     Greaves, G. N.; Dent, A. J.; Dobson, B. R.; Kalbitzer, S.; Pizzini, S.; Muller, G. *Physical Review B* **1992**, *45*, 6517.

(42)     Bevington, P. R.; Robinson, D. K. *Data reduction and error analysis*; McGraw-Hill: New York, 2003.

(43)     Taylor, J. R. *Error analysis*; Univ. Science Books: Sausalito, California, 1997.

(44)     Timoshenko, J.; Kuzmin, A. *Comput. Phys. Commun.* **2009**, *180*, 920.

(45)     El Osta, R.; Frigoli, M.; Marrot, J.; Medina, M. E.; Walton, R. I.; Millange, F. *Cryst. Growth Des.* **2012**, *12*, 1531.

(46)     Millange, F.; Medina, M. I.; Guillou, N.; Ferey, G.; Golden, K. M.; Walton, R. I. *Angew. Chem.-Int. Edit.* **2010**, *49*, 763.

(47)     Nangia, A.; Desiraju, G. R. *Acta Crystallogr. Sect. A* **1998**, *54*, 934.

(48)     Priola, E.; Volpi, G.; Rabezzana, R.; Borfecchia, E.; Garino, C.; Benzi, P.; Martini, A.; Operti, L.; Diana, E. *Inorg. Chem.* **2020**, *59*, 203.

(49)     Stavitski, E.; Goesten, M.; Juan-Alcaniz, J.; Martinez-Joaristi, A.; Serra-Crespo, P.; Petukhov, A. V.; Gascon, J.; Kapteijn, F. *Angew. Chem.-Int. Edit.* **2011**, *50*, 9624.

(50)     Van Vleet, M. J.; Weng, T. T.; Li, X. Y.; Schmidt, J. R. *Chem. Rev.* **2018**, *118*, 3681.

(51)    Alexandrov, E. V.; Virovets, A. V.; Blatov, V. A.; Peresypkina, E. V. *Chem. Rev.* **2015**, *115*, 12286.

(52)    Cairns, A. B.; Catafesta, J.; Levelut, C.; Rouquette, J.; van der Lee, A.; Peters, L.; Thompson, A. L.; Dmitriev, V.; Haines, J.; Goodwin, A. L. *Nat. Mater.* **2013**, *12*, 212.

(53)    Cui, G. L.; Cao, X. Y.; Fang, W. H.; Dolg, M.; Thiel, W. *Angew. Chem.-Int. Edit.* **2013**, *52*, 10281.

(54)    Fernandez, E. J.; Laguna, A.; Lopez-De-Luzuriaga, J. M. *Dalton Trans.* **2007**, 1969.

(55)    Lefebvre, J.; Batchelor, R. J.; Leznoff, D. B. *Journal of the American Chemical Society* **2004**, *126*, 16117.

(56)    Committee, I. S. a. C. *Error Reporting Recommendations: A Report of the Standards and Criteria Committee*, 2000.

(57)    Kido, D.; Uemura, Y.; Ariga-Miwa, H.; Takakuasgi, S.; Asakura, K. *e-J. Surf. Sci. Nanotec.* **2020**, *18*, 249.

(58)    Stalpaert, M.; Janssens, K.; Marquez, C.; Henrion, M.; Bugaev, A. L.; Soldatov, A. V.; De Vos, D. *ACS Catal.* **2020**, *10*, 9401.

(59)    Moreno, M. A.; Haukka, M.; Kallinen, M.; Pakkanen, T. A. *Appl. Organomet. Chem.* **2006**, *20*, 51.

(60)    Sun, D. R.; Gao, Y. H.; Fu, J. L.; Zeng, X. C.; Chen, Z. N.; Li, Z. H. *Chemical Communications* **2015**, *51*, 2645.